

## Episodic Antarctic Shelf Intrusions of Circumpolar Deep Water via Canyons

ELLIE Q. Y. ONG,<sup>a, b</sup> EDWARD DODDRIDGE,<sup>c</sup> NAVID C. CONSTANTINOU,<sup>d</sup>  
ANDREW McC. HOGG,<sup>d</sup> AND MATTHEW H. ENGLAND<sup>a</sup>

<sup>a</sup> Climate Change Research Centre, Australian Centre for Excellence in Antarctic Science, University of New South Wales, Sydney, NSW, Australia

<sup>b</sup> Australian Research Council Centre of Excellence for Climate Extremes, University of New South Wales, Sydney, NSW, Australia

<sup>c</sup> Australian Antarctic Program Partnership, Institute for Marine and Antarctic Studies, University of Tasmania, nipaluna / Hobart, Tasmania, Australia

<sup>d</sup> Research School of Earth Sciences & Australian Research Council Centre of Excellence for Climate Extremes, Australian National University, Canberra, ACT, Australia

**ABSTRACT:** The structure of the Antarctic Slope Current at the continental shelf is crucial in governing the poleward transport of warm water. Canyons on the continental slope may provide a pathway for warm water to cross the slope current and intrude onto the continental shelf underneath ice shelves, which can increase rates of ice shelf melting, leading to reduced buttressing of ice shelves, accelerating glacial flow and hence increased sea level rise. Observations and modelling studies of the Antarctic Slope Current and cross-shelf warm water intrusions are limited, particularly in the East Antarctica region. To explore this topic, an idealised configuration of the Antarctic Slope Current is developed, using an eddy-resolving isopycnal model that emulates the dynamics and topography of the East Antarctic sector. Warm water intrusions via canyons are found to occur in discrete episodes, with large onshore flow induced by eddies. The episodic nature of cross-shelf warm water transport is demonstrated, with canyon width playing a key role in modulating cross-shelf exchanges; warm water transport through narrower canyons is more irregular than transport through wider canyons. The episodic cross-shelf transport is driven by a cycle of rising and falling rates of eddy generation in the Antarctic Slope Current, a variability intrinsic to the slope current that can be explained without any temporal variability in external forcings. Improved understanding of the intrinsic variability of warm water intrusions can help guide future observational and modelling studies in the analysis of eddy impacts on Antarctic shelf circulation.

### 1. Introduction

The Antarctic Slope Current (ASC) is a westward flowing current around Antarctica, lying close to the coast on the continental shelf. The ASC is characterised by steeply sloping isopycnals, which are located over the Antarctic continental slope, between the saline open ocean and the fresher Antarctic continental shelf. A key water mass of the saline open ocean is the Circumpolar Deep Water (CDW), which is largely a by-product of North Atlantic Deep Water with lesser contributions from adjacent water masses (e.g. Heywood et al. 2014; Thompson et al. 2018; Morrison et al. 2020; Daae et al. 2020). The poleward transport of this warm CDW is regulated by the slope current; depending on the local structure of the ASC, CDW can flood on to the continental shelf in intrusions, transporting heat poleward to the Antarctic shelf. This process can induce basal melt of ice shelves and increase glacial and ice sheet flow, resulting in global sea level rise (Depoorter et al. 2013; Hattermann et al. 2014; Herraiz-Borreguero et al. 2016; Rintoul et al. 2016; DeConto and Pollard 2016; Gudmundsson et al. 2019).

Given the significant impact Antarctic ice shelf melt can have globally, the extent to which CDW intrudes underneath the East Antarctic Ice Sheet is a major concern. The East Antarctic Ice Sheet holds a total sea-level equivalent

of 50m, an order of magnitude larger than that of the West Antarctic Ice Sheet (Stokes et al. 2022). However, much less research has been conducted in the East Antarctic compared to the West Antarctic region (Morlighem et al. 2020; Stokes et al. 2022). The East Antarctic Ice Sheet has previously been thought to be stable, with landlocked sectors that are not directly impacted by CDW intrusions and past melt rates that have been lower than those in the West Antarctic (e.g. Paolo et al. (2015); Stokes et al. (2022)). However, recent studies point towards a greater mass loss than previously predicted, especially in marine-based sectors of the East Antarctic Ice Sheet exposed to CDW intrusions onto the continental shelf (e.g. Rignot et al. (2019); Stokes et al. (2022)), highlighting the vulnerability of the East Antarctic Ice Sheet to melting due to warm water intrusions.

The sloped isopycnals of the ASC in East Antarctica are generally thought to act as a barrier between CDW offshore and the continental shelf, however, the presence of canyons in the topography on the continental shelf may provide a pathway for CDW flow on to the shelf. Oceanic observations have shown the presence of warm CDW intrusions through canyons in East Antarctica (Rintoul et al. 2016; Nitsche et al. 2017; Silvano et al. 2018, 2019; Hirano et al. 2020; Ribeiro et al. 2021; Herraiz-Borreguero and Naveira Garabato 2022). However, our physical understanding of these warm CDW intrusions via canyons is

Corresponding author: Ellie Q. Y. Ong, ellie.ong@unsw.edu.au

incomplete, as observations are scarce (e.g. Peña-Molino et al. 2016; Herraiz-Borreguero et al. 2016) and modelling studies are also limited, as outlined below.

Existing modelling studies do not generally take into account all the key factors that influence how CDW intrusions occur on the East Antarctic continental shelf. Namely, these studies do not generally resolve eddies, canyons and East Antarctica in the same model. Many regional modelling studies of the East Antarctic continental margin are not fully eddy-resolving (e.g. Gwyther et al. (2014, 2018); Nakayama et al. (2021)), even though eddies are crucial in governing the transport of CDW onto the continental shelf (Nøst et al. 2011; Thompson et al. 2014; Stewart and Thompson 2015). Conversely, existing eddy-resolving studies do not generally investigate the East Antarctic region and the associated ‘fresh shelf regime’, where strong easterly winds result in the poleward Ekman transport of cool, surface water, the incropping of density surfaces and a strong ASC (e.g. Thompson et al. (2018)). Instead, eddy-resolving modelling studies, such as the ones by Daae et al. (2017) and Liu et al. (2017), generally focus on ‘dense shelf regime’ regions of the Antarctic margin, where dense shelf water formation in polynyas leads to the formation of Antarctic Bottom Water (e.g. Williams et al. (2010); Ohshima et al. (2013)). These dense shelf water formation regions have different circulation regimes and dynamics compared to most of the East Antarctic margin (Darelius et al. 2014, 2016; Daae et al. 2017; Morrison et al. 2020). The only eddy-resolving modelling study of the fresh shelf regime that investigates CDW intrusions via canyons focuses on the mechanisms of cross-shelf exchange in a single topographic configuration (Liu et al. 2022). Currently, there are no eddy-resolving modelling studies investigating the effect of a range of canyons on the ASC and CDW intrusions in a fresh-shelf regime, hence our understanding of CDW intrusions under different configurations remains poor. Addressing this question is therefore the focus of the present study.

Here, we explore warm CDW intrusions through canyons in an idealised configuration based on the East Antarctic continental margin, using a range of canyon configurations. We model the fresh shelf regime dominant around the East Antarctic margin using an idealised eddy-resolving primitive equation model with isopycnal coordinates. The model is forced by wind stress at the surface, with restoring boundary conditions to the north. Using isopycnal coordinates allows us to model the stratification of the ASC with few vertical layers at a minimal computational cost, which makes it feasible to explore the parameter space of canyon geometries in eddy-resolving simulations. Further details about the model setup are given in Section 2. In Section 3, we investigate the intrinsically episodic intrusions of CDW onto the shelf, showing the effect of canyon geometry on the regularity of these intrusions, and that

the episodic variability of intrusions is linked to an intrinsic temporal variability of the ASC itself. In Section 4, we examine the intrinsic temporal variability of the ASC and develop a simplified low-order model that is able to reproduce episodic variability based on energy exchanges between different reservoirs. In Section 5, we discuss the implications of our results and future work.

## 2. Model setup

The model domain and forcings are designed to reproduce the fresh shelf regime (Thompson et al. 2018), and are inspired by the configuration used by Constantinou and Hogg (2019). We use the Modular Ocean Model version 6 (MOM6) (Adcroft et al. 2019) to solve the hydrostatic Boussinesq primitive equations in isopycnal coordinates. We have a zonally re-entrant channel on a beta-plane, with a zonal extent of 1000km, meridional extent of 500km, and maximum depth of 3km, that includes topography of a continental slope. The height of the continental slope, from the top of the sill on the edge of the continental shelf to the bottom, is 2.5km. The Coriolis parameter is  $f = f_0 + \beta y$ , with  $f_0 = -10^{-4} \text{ s}^{-1}$ ,  $\beta = 1.5 \times 10^{-11} \text{ m}^{-1} \text{ s}^{-1}$  and  $y$  is distance from centre of the channel in the latitudinal direction. These values are typical of the Southern Ocean but the gradient in planetary vorticity has a smaller contribution to the dynamics than the effective beta induced by topography. Momentum is removed from the bottom isopycnal layer via quadratic drag with a drag coefficient of  $c_{\text{drag}} = 0.003$ .

The idealised model configuration is informed by the neutral density profiles and zonal velocities of sections of the ASC from global ocean-sea ice model simulations using the ACCESS-OM2-01 global ocean-sea ice model and from previous idealised experiments (Stewart and Thompson 2015, 2016; Huneke et al. 2019; Kiss et al. 2020). We use four density layers to represent the slope current region: two layers of Antarctic Surface Water, a Circumpolar Deep Water (CDW) layer and a Dense Shelf Water layer. The density values used in each of the layers are  $\rho_1 = 1027.8 \text{ kg m}^{-3}$ ,  $\rho_2 = 1028.0 \text{ kg m}^{-3}$ ,  $\rho_3 = 1028.1 \text{ kg m}^{-3}$ ,  $\rho_4 = 1028.3 \text{ kg m}^{-3}$ , and were based on neutral density values from Stewart and Thompson (2015). The model domain is shown in Figure 1 (a), with a snapshot of the top surface water isopycnal layer, CDW layer, and dense shelf water layer. Density interfaces are restored at the northern boundary to mimic the open ocean. The initial stratification (before spin-up) has a first Rossby deformation radius of 5km on the shelf and 11km offshore, thus eddies are comfortably resolved by our simulations which have a 1km lateral resolution. We experimented with a 2km resolution configuration but it did not fully resolve the eddying behaviour in the ASC. A preliminary test on doubling the resolution to 0.5km showed little qualitative change in ASC transport and CDW intrusions.

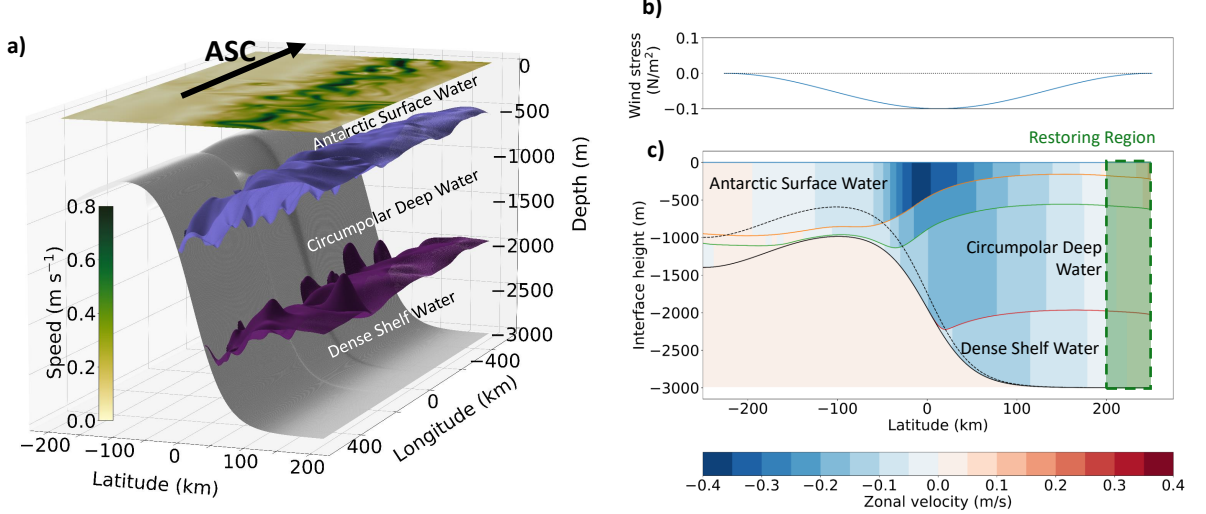


FIG. 1. (a) Snapshot of isopycnal interfaces for the upper surface water, CDW and dense shelf water layers in the control simulation of the ASC, with the widest steep-sided canyon topography. Instantaneous surface speed is shown on the top isopycnal interface. (b) Profile of zonal wind stress forcing, applied at the surface. (c) Cross-sectional profile of isopycnal surfaces in the centre of the canyon between each of the four density layers: upper and lower surface water, CDW, and dense shelf water. Colours in each density layer represent the 10-year mean zonal velocity in each layer. Black dashed line shows the topography of the continental slope away from the canyon, while the black solid line shows the topography of the continental slope at the centre of the canyon. The restoring region where density interfaces are relaxed to a set height at the northern boundary, representing the open ocean, is shown in green. The densities of each isopycnal layer are, starting from the surface layer,  $\rho_1 = 1027.8 \text{ kg m}^{-3}$ ,  $\rho_2 = 1028.0 \text{ kg m}^{-3}$ ,  $\rho_3 = 1028.1 \text{ kg m}^{-3}$ ,  $\rho_4 = 1028.3 \text{ kg m}^{-3}$ .

The wind stress forcing is steady and zonally symmetric, with only zonal wind forcing. We use a maximum wind stress input of  $\tau_0 = 0.1 \text{ N m}^{-2}$  for the control simulation, as in the fresh shelf regime example (Stewart and Thompson 2015). The zonal wind stress,  $\tau_x$ , is

$$\tau_x = -\tau_0 \cos^2(\pi y / \sigma_\tau), \quad (1)$$

where  $\sigma_\tau = 500 \text{ km}$  is the width of the channel, also the width of the wind stress forcing profile. The zonal wind profile for the control simulation is shown in Figure 1 (b).

We add canyons to the continental slope topography to investigate how their presence influences shoreward transport of CDW onto the continental shelf. The canyon geometries in this investigation are idealised: we use a steep-sided canyon, shaped like a trough, or a canyon with sloped-sides of a Gaussian-shape. Figure 1 (a) shows the topography for a steep-sided canyon of 200 km width. Simulations were run using canyons of width 20 km, 50 km, 100 km, 150 km and 200 km for the full-width half maximum for the steep-sided and Gaussian canyon cases, and with a depth of 400 m on the continental shelf. The widths of the canyons are comparable to cross-sectional widths of canyons observed around the Antarctic Margin, as shown in Figure 2 and were chosen from the ETOPO1 Global Relief Model (NOAA National Geophysical Data Center 2009). The topography of the continental slope is additionally based on

previous idealised experiments and the ACCESS-OM2-01 model (e.g. Stewart and Thompson 2015; Kiss et al. 2020)).

After equilibration, a snapshot of the stratification of the idealised fresh shelf regime is shown in Figure 1 (a), for the control simulation with the steep-sided canyon of 200 km width, the widest canyon modelled. Statistical equilibrium was typically reached after 20 years, with daily mean data for analysis taken from at least a 20 year long period of statistical equilibrium. A strong westward current is spun up in the surface layers with a maximum zonal velocity of  $0.3 \text{ m s}^{-1}$  in the water column, when averaged over 10 years, shown in Figure 1 (c). ASC velocities in this simulation are slightly higher than velocities in other models and observations. For example, Hunekte et al. (2022) showed a maximum zonal velocity of  $0.2 \text{ m s}^{-1}$  in the water column in a region of the fresh shelf regime, when averaged over 10 years, while a regional model of the ASC showed maximum instantaneous zonal velocities off the Totten Ice Shelf in East Antarctica to be  $0.2 \text{ m s}^{-1}$  (Nakayama et al. 2021). In our simulation, density surfaces are steeply sloped and incrop into the continental slope, consistent again with regions in the fresh shelf regime. Although idealizations are made in the configuration so that eddies can be resolved and a wide parameter space can be explored, this control simulation still exhibits the key features characteristic of the fresh shelf regime and East Antarctica, and is used

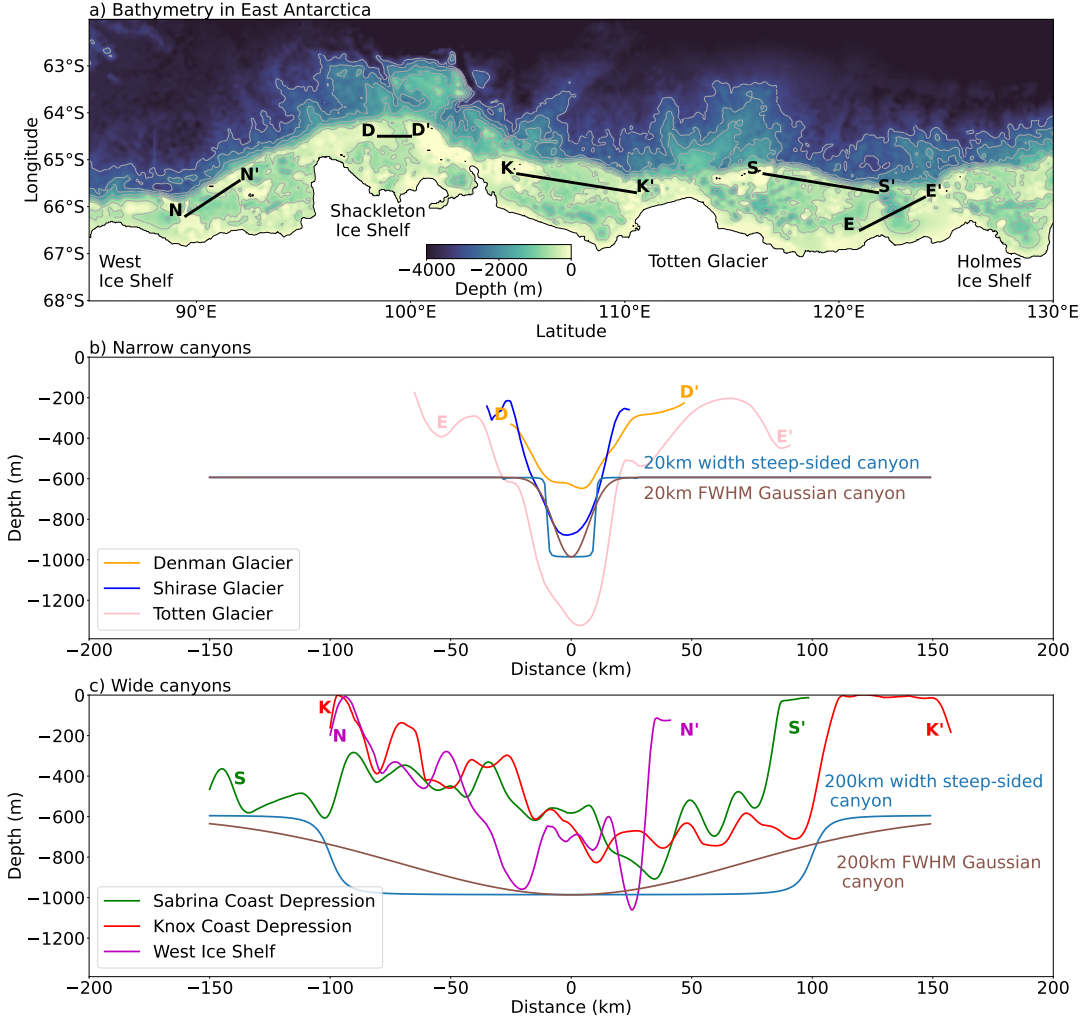


FIG. 2. (a) Observed bathymetry in the East Antarctic, using ETOPO1 data (NOAA National Geophysical Data Center 2009), with sampled canyon cross-sections marked in black. Contours of 500m, 1000m, 1500m and 2000m depth are marked in grey. (b) Cross-sections of observed narrow canyons taken from (a), labelled by name or associated glacier. The Shirase glacier canyon is not shown in (a) as it is outside the domain pictured in (a). Cross-sections of idealised narrow canyons are shown in the steep-sided (blue) and Gaussian (brown) shapes. (c) Cross-sections of observed wide canyons taken from (a), labelled by name or associated glacier. Cross-sections of idealised wide canyons are shown in the steep-sided (blue) and Gaussian (brown) shapes.

as a basis for exploring how CDW intrusions access the Antarctic continental shelf through canyons.

### 3. Temporal variability of CDW intrusions and the ASC

We start by looking at the qualitative behaviour of on-shelf intrusions in the control simulation of Figure 1. We choose the control simulation as this is the canyon configuration which allows for the largest CDW intrusions,

and it typifies canyon geometry at certain locations around the East Antarctic sector (Figure 2 (c)). We are primarily interested in meridional transport of CDW, hence the time series in Figure 3 (a) shows meridional transport in the CDW layer at the sill latitude across a section of the canyon (see dotted line in Figure 3 (b)), with poleward transport shown as negative. Since there is no water mass transformation on the shelf, the CDW shelf exchange is balanced over a long time period. However, this time series shows

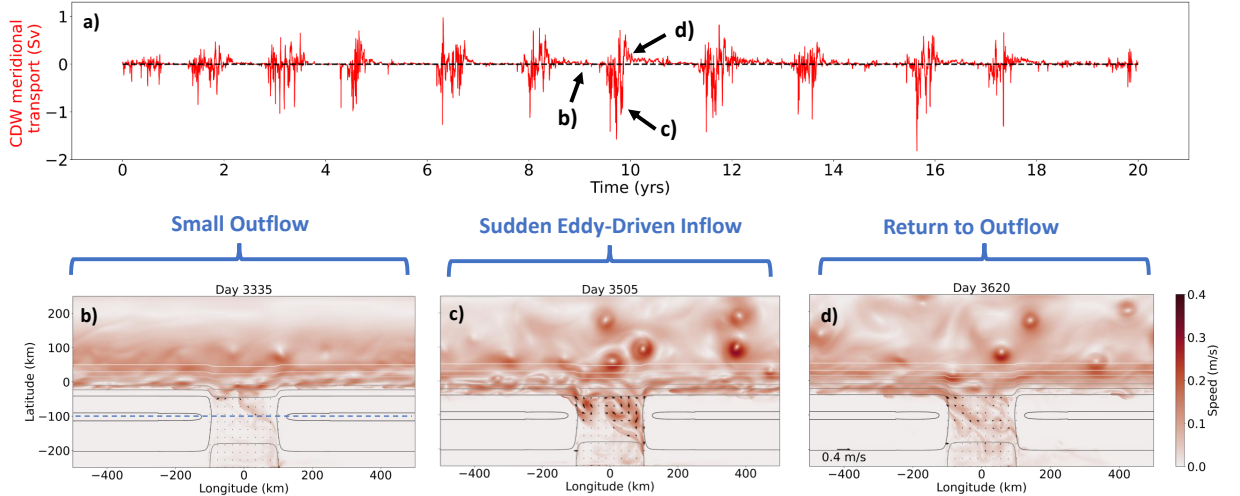


FIG. 3. (a) Meridional transport of CDW across a cross-section of canyon at latitude  $y = -100$  km in the control simulation over 20 years at equilibrium. The cross-section is taken across the blue dashed line in (b). Snapshots of speed in the CDW layer of simulation showing the different stages of episodic CDW intrusion: (b) a small outflow of CDW flowing off the continental shelf, (c) a sudden eddy-driven inflow onto the continental shelf, and (d) a return to a CDW outflow. We see that eddies form in the ASC and drive a large onshore flow approximately every two years. The eddies on the continental shelf then begin to dissipate and flow offshore, continuing on the cycle of CDW intrusions.

that there is poleward meridional transport of CDW in the canyon, and that this cross-shelf transport is not constant but instead occurs in isolated episodes approximately every two years. The different stages of CDW intrusion are highlighted in snapshots of speed in the CDW layer over time, shown in separate stages of Figure 3 (b), (c) and (d). The most common state of the system is the small outflow state of little cross-shelf exchange as indicated in Figure 3 (b), with a minimal amount of CDW draining off the continental shelf. There is then a transition to a stronger eddy field in the ASC, corresponding with a stage of sudden eddy-driven flow of CDW onshore, with coherent vortices reaching the continental shelf as seen in Figure 3 (c). While CDW pools on the continental shelf, eddies in the ASC weaken, and CDW begins to flow offshore, returning to the original state of primarily offshore transport of CDW as indicated in Figure 3 (d). This entire cycle of weak CDW offshore flow, followed by a sudden shoreward flow, and a return to an offshore flow is surprising given that the simulated ASC has reached a statistically steady state. Additionally, as wind and sponging of layer interfaces remain constant throughout the simulation, this interannual variability of episodic CDW intrusions is not the result of external forcings, pointing to the presence of intrinsic temporal variability. Understanding this CDW transport variability is the focus of the rest of this section, initially analysing the effect of canyon width on the variability of CDW intrusions, then investigating the origins of the CDW variability.

#### a. Effect of canyon width on warm water intrusions

We observe in the control simulation the intrinsically episodic behaviour of CDW intrusions through a canyon, and see in Figure 3 that the canyon is a key pathway by which CDW reaches the continental shelf. Hence we aim to understand how characteristics of the canyon, specifically the width of the canyon, affect the episodic poleward flow of CDW. We first compare the narrowest (20 km width) and widest (200 km width) steep-sided canyon cases of the simulations we have run. The time series of meridional CDW transport at the sill latitude is plotted in Figure 4, with the time series for the narrow canyon case in (a) and that of the widest canyon case in (c). Qualitatively, the narrower canyon case shows more isolated instances of CDW intrusions highlighted by circles in Figure 4 (a). However, CDW intrusions in the wider canyon case last for a longer period of time, instead of the isolated single bursts of CDW travelling onto the shelf in the narrow canyon case, shown in the ovals on Figure 4 (c). A plot of the probability density function for meridional CDW transport using 50 years of daily data reveals a long tail of large poleward transports in the narrow canyon case. (Figure 4 (b) for the narrow 20 km and (d) wide 200 km case). The long tail of large transports originates from the isolated pulses of CDW in the narrow canyon case and cause the distribution of meridional CDW transport to be heavily skewed. Hence, a topographic configuration with more asymmetric, or irregular, CDW intrusions has a more negatively skewed distribution of meridional CDW transport.

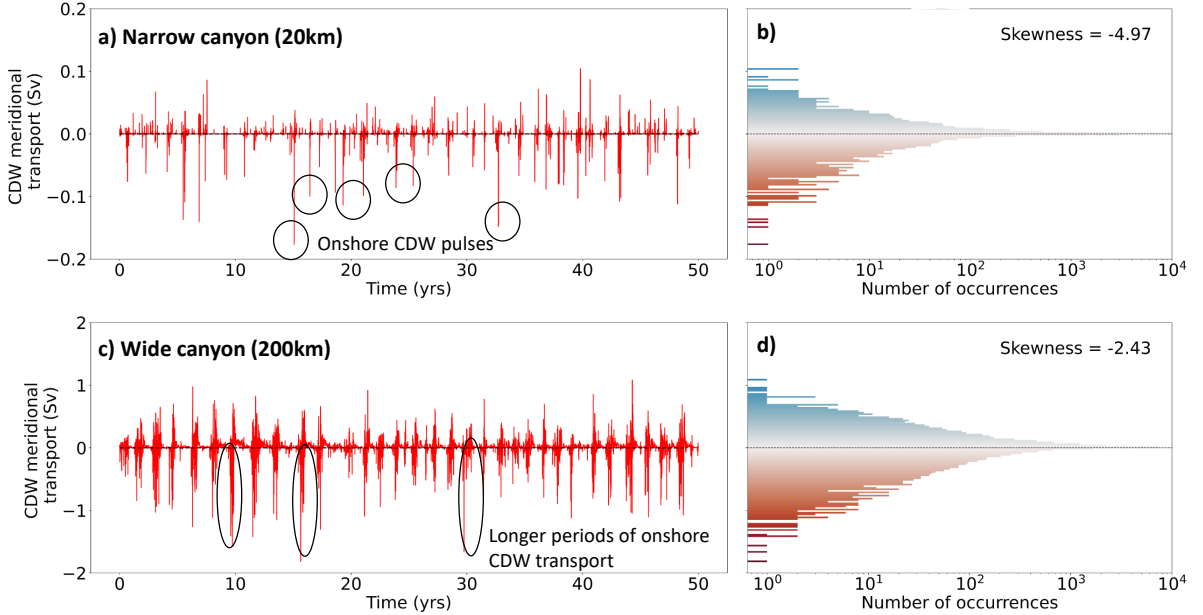


FIG. 4. (a) Meridional transport of CDW across latitude  $y = -100$  km and (b) probability density function of meridional transport of CDW across the same latitude for the narrow 20km wide steep-sided canyon case. (c) and (d) show the same quantities as (a) and (b) respectively but for the wide 200km steep-sided canyon case. Skewness values of meridional CDW transport indicate that a more negatively skewed distribution has more irregular and episodic CDW intrusions.

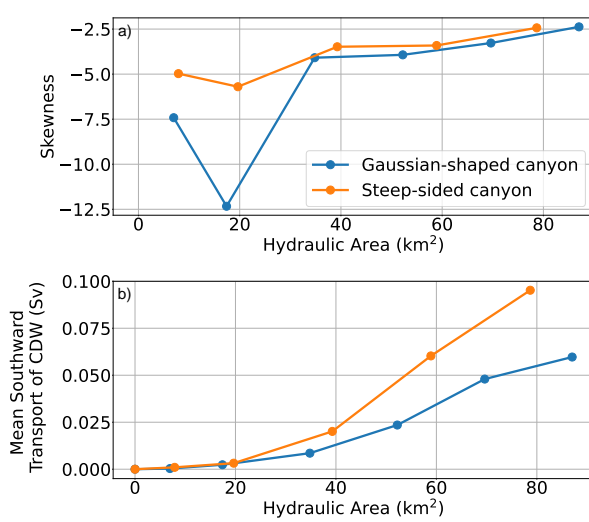


FIG. 5. (a) Skewness of meridional CDW transport distribution as in Figure 4 with hydraulic area of canyon, for canyons of steep-sided and Gaussian-shapes. A more negatively skewed distribution has a more asymmetric distribution and irregular CDW transport. (b) Mean southward transport of CDW across latitude  $y = -100$  km with hydraulic area of canyon for canyons of steep-sided and Gaussian-shapes. Canyons with a larger hydraulic area allow for a greater transport of CDW poleward and more regular intrusions.

To directly compare the regularity of CDW transport across different canyon widths, we use the skewness metric to quantify the asymmetry of CDW flow on and off the shelf. The results of this comparison are shown in Figure 5 (a), plotting the skewness, analogous to the regularity of intrusion, against the hydraulic area of the canyon. For the steep-sided canyon experiments (orange line), we find that narrower canyons have a more negatively skewed distribution of meridional CDW transport, and thus more asymmetric CDW transport. Narrow steep-sided canyons have sudden large intrusions but more frequent instances of small CDW drainage, while wider steep-sided canyons exhibit less asymmetry between the CDW drainage and intrusions onto the shelf. Observed canyons do not always have geometries comparable to the steep-sided case, so we conducted the same analysis for experiments with canyons of a more gently-sloped Gaussian-shape with varying width, plotted in blue in both panels of Figure 5, where we confirm that the same overall trend in episodic behaviour with canyon width holds as in the steep-sided canyon cases.

Alongside understanding the nature of CDW intrusions and its variability, we also compare poleward CDW transport between different canyon configurations. We select the southward transport values of CDW at the sill latitude, zero out any northward transport, and zonally-integrate the southward transport at each time step before taking the

temporal mean over 50 years of daily data. The time-mean southward transport of CDW is computed in simulations with a range of canyon widths and canyon geometries, including a simulation without a canyon on the continental slope, as seen in Figure 5 (b). Across both canyon geometries, southward transport of CDW onto the shelf increases with the hydraulic area available for flow onto the shelf. Note that in the simulation without a canyon, there is no southward transport of CDW across the sill latitude, highlighting the importance of canyons in CDW intrusions. Additionally, canyon configurations with steep-sided canyons have a greater southward transport of CDW than those with a Gaussian-shape shown in blue in Figure 5 (b), even when canyons with the same hydraulic area are compared. We conclude that wider canyons allow for more CDW transport onto the shelf, with less asymmetry in meridional CDW transport when compared to narrower canyons, and this result is robust for the two canyon geometries tested.

The effect of canyon width on the regularity of CDW intrusions can affect the predictability of the East Antarctic Margin: although narrow canyons allow for less CDW transport poleward, the asymmetry towards intrusions and the key locations of narrow canyons, e.g. beneath the Denman Glacier, may indicate that further study into cross-shelf dynamics across narrow canyons is required in order to predict the variability of warm water intrusions onto the shelf where vulnerable ice shelves sit. Wider canyons allow for greater CDW transport, with intrusions occurring periodically at a set frequency, which may make flow at these wider canyons easier to predict. We next investigate the mechanisms governing the periodic behaviour of CDW intrusions.

### b. Link between CDW intrusions and ASC variability

Although we have found an intrinsic temporal variability of CDW intrusions across a range of canyon geometries, the mechanisms governing the variability are unclear. We can nonetheless see a connection between the variability of CDW intrusions and the ASC strength in Figure 6 (a), where the strength of the ASC is plotted in blue and the meridional CDW transport in red, both plotted for 20 years at statistical equilibrium. In the control simulation with the widest canyon, the ASC strength varies from 40-80 Sv with a mean of around 60 Sv, larger than the ASC strengths observed by Peña-Molino et al. (2016), which varies between 0-100 Sv of westward transport with a mean of around 20 Sv. The ASC strength exhibits variability on an interannual time-scale, and in this control simulation, the poleward transport of CDW is maximised when the slope current is weaker. This is consistent with the results by Nakayama et al. (2021) and posits a link between episodic warm water intrusions and the ASC strength.

Intrusions of warm water onto the Antarctic continental shelf have previously been found to be driven by eddy activity (Nøst et al. 2011; St-Laurent et al. 2013; Hattermann et al. 2014; Stewart and Thompson 2015, 2016). To determine if the CDW intrusions arise from eddies in the ASC, we compute the area-integrated eddy kinetic energy (EKE) in the ASC in the CDW layer. We use a layered thickness-weighted framework (Young 2012), with energy transfers between eddy energy reservoirs as described by Aiki et al. (2016) and Yung et al. (2022). The time-mean EKE in  $i$ -th layer is  $\frac{1}{2}\rho_0 h_i |\mathbf{u}_i''|^2$ , where  $\rho_0$  is the reference density and we use the density of the top layer as the reference density,  $h_i$  is the thickness of layer  $i$ ,  $\mathbf{u}_i$  is the velocity in layer  $i$ , and  $\mathbf{u}_i'' = \mathbf{u}_i - \widehat{\mathbf{u}}_i^t$  is the deviation from the thickness-weighted mean velocity  $\widehat{\mathbf{u}}_i^t$ , where  $\widehat{\mathbf{u}}_i^t = \overline{h_i \mathbf{u}_i^t} / \overline{h_i}$ , with  $\langle \cdot \rangle^t$  a time-mean. The EKE is integrated over the ASC in the CDW layer, bounded by the latitudes of  $y = -50\text{km}$  and  $y = 100\text{km}$  and integrated across the whole channel in the zonal direction. Inspecting the time series of the EKE with the meridional volume transport of CDW in Figure 6 (b), plotted for 20 years at equilibrium, we observe that episodes of southward transport of CDW follow peaks in area-integrated EKE. The increased southward transport of CDW thus appears to be linked to a greater presence of eddies in the ASC, such that the temporal variability in rates of eddy generation could drive the intrusions of CDW.

To identify the mechanisms driving the temporal variability of EKE, we compute the baroclinic and barotropic contributions of energy conversion to EKE in the ASC (Aiki et al. 2016; Yung et al. 2022). The baroclinic energy conversion term,  $\overline{\mathbf{u}'_i \cdot (h_i \nabla \phi'_i)}$ , links the contribution of interfacial form stress to EKE in layer  $i$ , while the barotropic energy conversion term,  $\rho_0 (\widehat{\mathbf{u}}_i \cdot \nabla) \cdot (h_i \mathbf{u}'_i \otimes \mathbf{u}'_i)$ , is the contribution of Reynolds stress, and thus horizontal shear, to EKE. Here,  $\phi_i$  is the Montgomery potential and  $\phi'_i = \phi_i - \overline{\phi_i}$ , where  $\langle \cdot \rangle$  is a rolling mean over 200 days to smooth out transient eddy effects.  $\mathbf{u}'_i = \mathbf{u}_i - \widehat{\mathbf{u}}_i$  is the thickness weighted mean velocity computed using a rolling mean, where  $\widehat{\mathbf{u}}_i = \overline{h_i \mathbf{u}_i} / \overline{h_i}$ , and  $\otimes$  is the outer product of two vectors.

The baroclinic and barotropic energy conversions for the control simulation of the widest canyon are plotted in Figure 6 (c) for 20 years at equilibrium. The peaks in both the baroclinic and barotropic energy conversions precede peaks in warm intrusions, showing that the generation of eddies results in more CDW intrusions with a short time lag of days. Crucially, the baroclinic energy conversion term dominates the barotropic energy conversion term, highlighting the contribution of baroclinic instability to the EKE gain. Hence, this baroclinic instability is the mechanism by which eddies are generated to drive CDW intrusions on to the shelf.

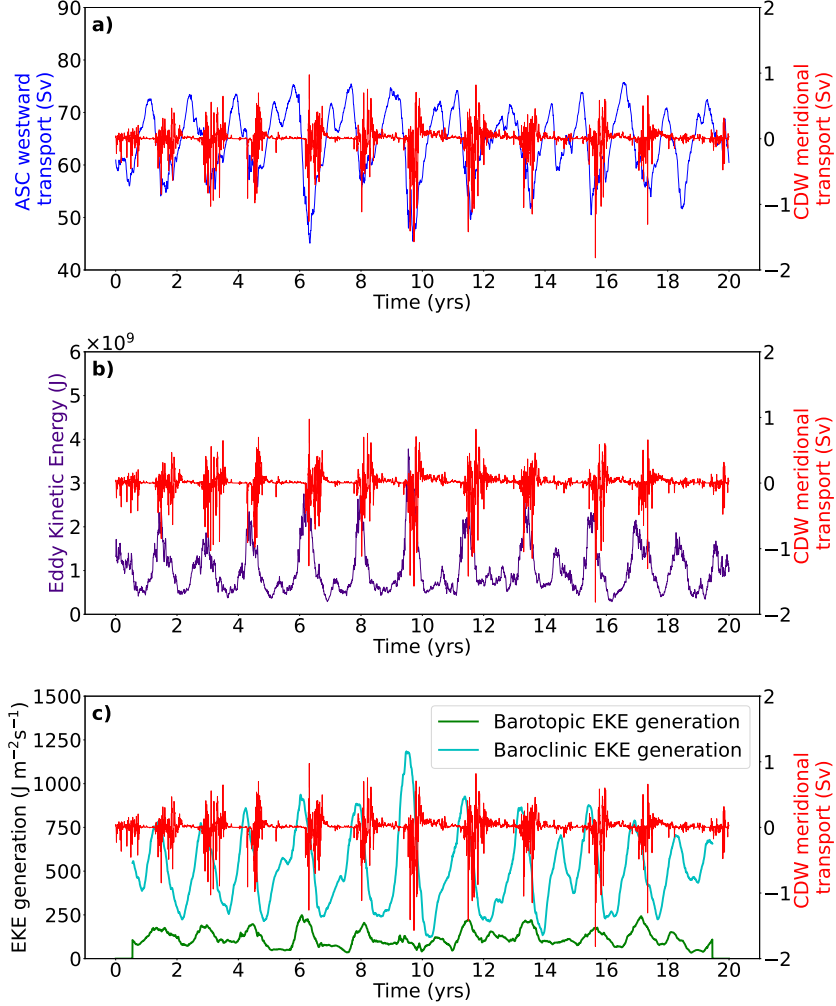


FIG. 6. (a) Time series of ASC strength and meridional volume transport of CDW onto shelf at latitude  $y = -100\text{km}$ . (b) Time series of EKE per unit area and the same CDW transport time series as in (a). (c) Time series of baroclinic and barotropic energy conversions per unit area and the same CDW transport time series as in (a). Energy conversions are calculated as a rolling average of 200 days. All time series are for 20 years after the flow has equilibrated. The episodes of meridional CDW transport coincide with weakening of the ASC, and precedes peaks in EKE and EKE generation by a short time lag of days.

We conclude that episodic generation of eddies through baroclinic instability weakens the ASC, while simultaneously driving the onshore transport of CDW. Previous work by Nakayama et al. (2021) has already shown a link between a weak ASC and warm CDW intrusions, and in this channel model, a weaker ASC is linked with warm CDW intrusions by the generation of eddies through baroclinic instability. The mechanism is further supported by experiments with increased bottom drag, under which eddy generation is reduced and CDW intrusions are simultaneously inhibited (not shown). As the variability of CDW intrusions originates from changes in the generation of eddies in the ASC, the ASC is therefore a key governing factor

of CDW intrusions whose intrinsic variability is crucial to be understood.

#### 4. Intrinsic ASC variability

In Section 3 we demonstrated that there is an intrinsic time-variability to CDW intrusions caused by a cycle of rising and falling rates of eddy generation in the ASC. However we did not address the origin of the variability in the ASC. In this section, we show that the cycle of rates of eddy generation in the ASC can be explained using a low-order model that describes the coupling of available potential energy and eddy kinetic energy, and that the model predicts an intrinsically oscillatory ASC. We also compare

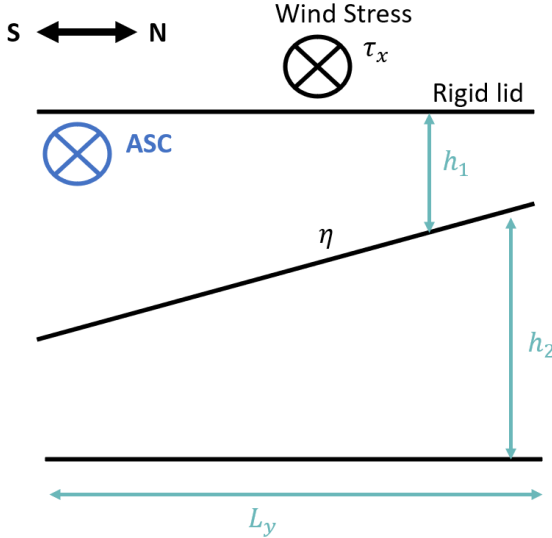


FIG. 7. Schematic showing features of the low-order model, replicating an ASC at equilibrium, with two density layers, a rigid lid, a sloping isopycnal of interface height  $\eta$  with a constant slope across the extent of the domain  $L_y$ , zonal wind stress input of  $\tau_x$ , layer thicknesses of each layer being  $h_1$  and  $h_2$  for top and bottom layers respectively. The wind input slopes the isopycnal interface and spins up a westward current.

the low-order model predictions to our isopycnal channel model simulations, firstly by comparing the energy evolution predicted by the low-order model to channel model simulations, followed by parameter sensitivity tests. These comparisons allow us to evaluate whether the physics of the low-order model can explain the key processes governing ASC time-variability in the fresh-shelf regime.

#### a. Low-order model and oscillatory solution to linearised equations

We demonstrated that the intrinsic variability of the idealised ASC in the fresh shelf regime arises from eddy generation via baroclinic instability. However, the rate of baroclinic eddy generation is not constant even at equilibrium, instead, baroclinic instability occurs in a periodic cycle. The cause of this cycle and its timescale are unclear as there are no time-varying external forcings to induce this oscillatory behaviour. Therefore, we aim to understand the equilibrated state better, prompting the use of a low-order model.

We postulate that the interannual variability in this system occurs due to energy exchange between total eddy energy and total available potential energy. To demonstrate this, we develop a low-order system that governs the evolution of total eddy energy, and total available potential energy in an idealised ASC, in order to understand the quasi-steady state of the ASC. We start with a two-layer, zonally symmetric isopycnal model of the ASC, pictured

in Figure 7, with constant zonal wind forcing. The fluid interface is assumed to have a constant slope. The energy budget of the system can be expressed as:

$$\frac{dE}{dt} = \text{eddy energy conversion} - \text{damping}, \quad (2)$$

$$\frac{dAPE}{dt} = \text{wind input} - \text{eddy energy conversion}, \quad (3)$$

where  $E = \sum_i \int (\frac{1}{2} \rho_0 h_i |\mathbf{u}_i''|^2 + \frac{1}{2} \rho_0 g' \eta''^2) dy$  is the depth-integrated total eddy energy per unit length in the longitudinal direction, where  $\eta$ , the isopycnal interface height, is defined relative to the initial interface height at the southern boundary and  $\eta'' = \eta - \bar{\eta}$ .  $APE = \sum_i \int \frac{1}{2} \rho_0 g' \eta^2 dy$  is the depth-integrated total available potential energy per unit longitudinal length, and damping is in the form of  $\lambda E$ , with  $\lambda$  the linear damping coefficient. Eddy energy conversion is  $|f|/N |\partial u/\partial z| E$  (following Marshall et al. (2017)), where  $f$  is the Coriolis parameter,  $N$  is the buoyancy frequency and  $u$  is the zonal velocity. Wind input per unit longitudinal length is given by  $\int \boldsymbol{\tau} \cdot \mathbf{u}_{\text{surface}} dy$ , where  $\boldsymbol{\tau}$  is the wind stress vector and  $\mathbf{u}_{\text{surface}}$  is the surface velocity.

We wish to express (2) and (3) as coupled differential equations in terms of  $APE$  and  $E$ , so we define the components of the equation in terms of these variables. We assume geostrophic velocities in each of the isopycnal layers, thermal wind balance, rigid lid, constant linear shear and zero bottom velocity. The zero bottom velocity is justified as bottom velocities in both our channel simulations and in observations around the East Antarctic are generally less than 10% of the surface velocities. The procedure for defining and discretising these terms for the case of the two-layer model is outlined in the Appendix, and we end up with the equations:

$$\frac{dE}{dt} = \underbrace{\frac{2}{NH} \sqrt{\frac{6g'}{\rho_0 L_y^3}} \sqrt{APE}}_a E - \lambda E, \quad (4)$$

$$\frac{dAPE}{dt} = \underbrace{\frac{2|\tau_x|}{|f|} \sqrt{\frac{6g'}{\rho_0 L_y}}}_b \sqrt{APE} - \underbrace{\frac{2}{NH} \sqrt{\frac{6g'}{\rho_0 L_y^3}} \sqrt{APE}}_a E, \quad (5)$$

where  $\rho_0$  is the reference density,  $g' = g \Delta \rho / \rho_0$  is reduced gravity of the two layer system,  $H$  is the total thickness of fluid,  $L_y$  is the latitudinal extent of the domain where the slope of the density surface is constant, and  $\tau_x$  is the zonal component of the wind stress input.

Now we have two coupled non-linear ordinary differential equations (4) and (5). To find the fixed points we set

$d/dt = 0$  and solve, setting the constants to  $a$  and  $b$  for simplicity. We get a non-trivial fixed point:

$$\sqrt{APE} = \lambda/a \quad \text{and} \quad E = b/a. \quad (6)$$

Upon linearising the energy equations (4)-(5) about the equilibrium (6), we obtain evolution equations for the deviations of  $E$  and  $APE$  about their equilibrium values. Combining these evolution equations we end up with:

$$\frac{d^2E}{dt^2} = -\frac{ab}{2}E, \quad (7)$$

which has oscillatory solutions of the form  $E \propto e^{i\omega t}$ , with

$$\omega = \sqrt{\frac{ab}{2}} = \frac{1}{L_y} \sqrt{\frac{12g'|\tau_x|}{|f|\rho_0 NH}}, \quad (8)$$

$$T = \frac{2\pi}{\omega} = \pi L_y \sqrt{\frac{\rho_0 NH |f|}{3g'|\tau_x|}}, \quad (9)$$

where  $\omega$  is the radial frequency of oscillation, and  $T$  is the period of the oscillation of  $E$  and  $APE$ .

The solution to the linearised equations about the fixed point is oscillatory, which is consistent with an intrinsically time-varying ASC. The oscillatory solution implies that the total eddy energy and available potential energy in the ASC will follow an oscillation with a steady period defined in (8), despite no timescale being imposed on the model through external forcing. The next section will compare the low-order model to the channel model simulations, such that conclusions about the underlying dynamics can be drawn between these system.

### b. Energy evolution in low-order model

The low-order model (4)-(5) describes the evolution of eddy energy and available potential energy in a current system, and when the system is close to equilibrium the low-order model acts as an oscillator. In order to evaluate the extent to which the low order model replicates the physics in the isopycnal channel model simulations, we compare key characteristics of the low-order model to the simulations. We solve the low-order model fully to obtain the time-evolution of energy reservoirs, starting from prescribed initial conditions. The predicted energy evolutions can then be compared to their corresponding quantities in the isopycnal channel model simulations.

Although the linearised low-order model does show an oscillation consistent with the channel model simulations, there are a number of assumptions in the low-order model that do not hold in the simulation, making direct comparisons difficult. For example, the low-order model assumes a constant slope of the density interface throughout the slope current and a linear drag, while the isopycnal channel simulations have a varying interfacial slope

and quadratic drag. Additionally, the simulations feature continental slope topography while the low-order model assumes a flat-bottom channel. The lack of topographic variation in the low-order model implies that all wind stress input has to be balanced by bottom drag, rather than being balanced by topographic form stress in a setup with bathymetric features (Munk and Palmén 1951). Hence if both setups were to have similar equilibrated zonal transport values, then the low-order model would require much higher values of drag as it does not have any other way to dissipate zonal momentum. Expecting high values of  $\lambda$  in the low-order model, we choose  $\lambda = 5 \times 10^{-7} s^{-1}$  as this gives us energy values comparable to the control simulation in Figure 8, and we use this bottom drag parameter to solve the non-linear energy equations of the low-order model.

Solving the initial value problem for the non-linear energy equations in (4) and (5) using the chosen bottom drag parameter, with the initial energy of 1.05 times the equilibrium energy values (6), we find that the theoretical solution for  $E$  and  $APE$  from the low-order model (Figure 8 (a)) is comparable to the  $E$  and  $APE$  time series calculated from the experimental data (Figure 8 (b)). In the low-order model solutions,  $APE$  increases before  $E$  and begins to drop off once  $E$  starts to increase. This is similar behaviour to that seen in the channel model simulations, where  $APE$  gain precedes the increase in  $E$  as plotted in Figure 8 (b), supporting the mechanism that  $APE$  is being converted into eddy energy via baroclinic instability. A discrepancy between the solution to the initial value problem and the time series of energies from channel model simulations is the period of the oscillation. Although both plots in Figure 8 show a cycle of regular oscillations, the period of oscillation in the channel model simulations is longer than that expected from the low-order model. Later in this section we show that the period of oscillation predicted by the low-order model is consistently shorter than that in the channel model simulations, and we also investigate the trends in the period of oscillation as experimental parameters are varied.

### c. Parameter sensitivity tests in the low-order model

Having evaluated the solutions to the low-order model, showing the time-evolution of the eddy energy reservoirs, we now investigate how changing parameters affects the predictions of the low-order model. In particular, we look at how predictions for period and equilibrium energies scale with parameters relevant to a changing ASC, and compare these predictions with the isopycnal channel model simulations. In the solution to the linearised energy equations (8), the frequency of the intrinsic oscillation is proportional to  $\sqrt{\tau_x}$  but independent of linear bottom drag  $\lambda$ . Additionally, the equilibrium energies in the low-order model (6),  $E_0$  and  $APE_0$ , are proportional to wind stress

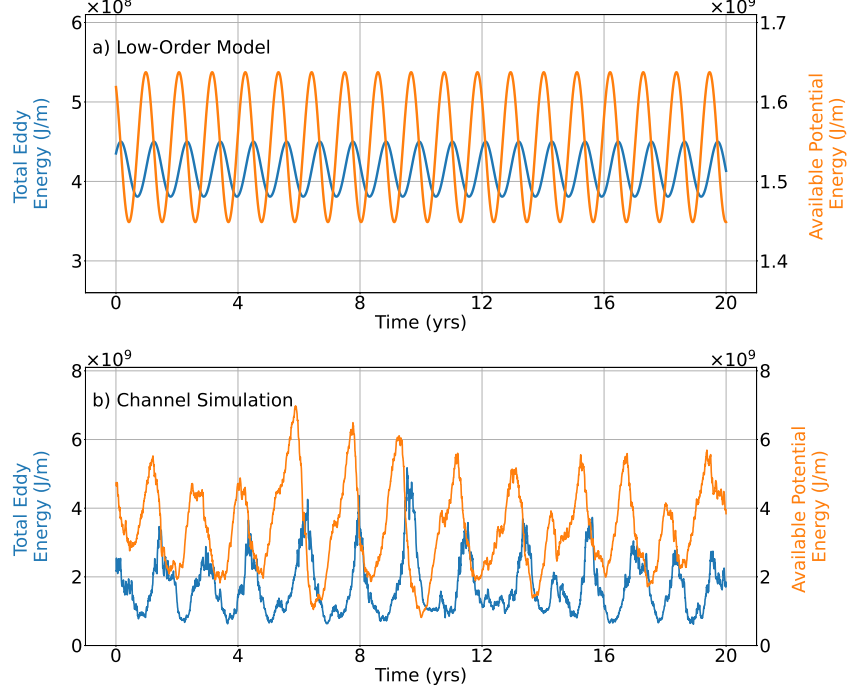


FIG. 8. (a) Solution to initial value problem of the low-order model, using  $\lambda = 5 \times 10^{-7} \text{ s}^{-1}$ . (b) Diagnostics of Eddy Energy and Available Potential Energy, calculated using 20 years of data at equilibrium from the control channel simulation (widest 200km steep-sided canyon).  $E$  is calculated in the CDW layer, and  $APE$  is calculated at the interface between the CDW layer and the lower surface water layer in the channel model simulations. Although the time-series has a period greater than that predicted around the equilibrium state using the low-order model, the  $APE$  similarly peaks and declines before  $E$  begins to increase as eddies are being generated.

input  $\tau_x$  and bottom drag squared,  $\lambda^2$ . Testing the parameter sensitivity of the channel model simulation as informed by the low-order model is significantly simpler and allows us to assess how the oscillation in the simulated ASC is affected by changing environmental conditions, hence, the focus on the effect of wind stress and bottom drag.

We modify wind stress and bottom drag in our layered model of the fresh shelf regime to test the dependence of the oscillation period and equilibrium energies on these parameters and verify the energy equations of the low-order model. We conducted four additional simulations for wind stress, at  $\tau_0 = 0.025, 0.05, 0.075, 0.125 \text{ N m}^{-2}$ , and five for bottom drag, with the quadratic drag coefficient at  $c_{\text{drag}} = 0.0015, 0.0024, 0.0036, 0.0045, 0.006$ , corresponding to a halving, 20% decrease, 20% increase, 50% increase and doubling of the control simulation's bottom drag coefficient. All these simulations utilise the topography of the widest canyon in the control simulation shown in Figure 1, as it exhibits the most regular periodic oscillation in ASC strength in our experiments and thus is the best comparison to the low-order model.

According to linear stability analysis of the low-order model equilibrium, the oscillation period is expected to decrease as wind stress is increased, but is independent

TABLE 1. Experimental parameters used in the low-order model.

Parameter	Value
$\tau_x$	$0.05 \text{ N m}^{-2}$ (domain-averaged of (1))
$H$	3000 m
$\rho_0$	$1027.8 \text{ kg m}^{-3}$
$\Delta\rho$	$0.5 \text{ kg m}^{-3}$
$L_y$	25 km
$h_1$	500 m
$h_2$	2500 m
$N$	$9.54 \times 10^{-4} \text{ s}^{-1}$
$\lambda$	$5 \times 10^{-7} \text{ s}^{-1}$

of bottom drag. Fourier spectral analysis was conducted on the eddy kinetic energy time series in each experiment. The dominant frequency was selected and its period is plotted in orange for each of the channel model simulations in Figure 9, with (a) for simulations varying wind stress, and (b) for simulations varying bottom drag. The period predicted by the low-order model (8) is shown in blue, and we have substituted values from the channel model simulations to estimate the period and conduct the parameter

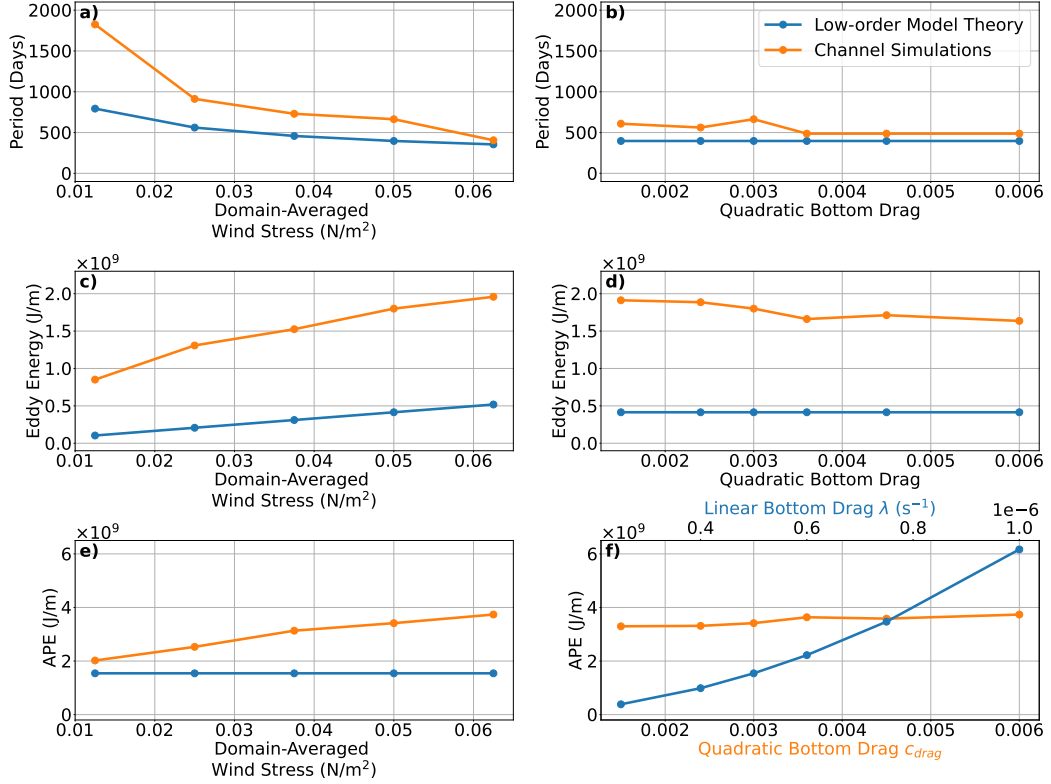


FIG. 9. Period of oscillation in  $E$  from the channel model simulations and in the low-order theory, with varying wind stress (a) and bottom drag (b). Magnitude of equilibrium Total Eddy Energy from the channel model simulations and in the low-order theory, with varying wind stress (c) and bottom drag (d). Magnitude of equilibrium Available Potential Energy from the channel model simulations and in low-order theory, with varying wind stress (e) and bottom drag (f).

sensitivity tests (see Table 1). We find that the period in the channel model simulations decreases as the strength of the wind forcing increases, but is independent of bottom drag, as predicted by the linearisation of the low-order model. The channel model simulations show a period systematically greater than that in the low-order model, which is consistent with Figure 8 where the control simulation has a longer oscillation period in energy than in the low-order model. Regardless, the trends seen in the low-order model still hold in the channel model simulations as wind stress and bottom drag are varied.

In addition to the period of  $E$  and  $APE$  oscillations, the low-order model parameters can also be used to predict the equilibrium values of  $E$  and  $APE$  and how they behave as wind stress and bottom drag are varied. The equilibrium values of the  $E$  and  $APE$ ,  $E_0$  and  $APE_0$ , are proportional to the wind stress input,  $\tau_x$ , and the square of the bottom drag  $\lambda^2$  respectively, as in (6). The equilibrium values for en-

ergy were found by taking a spatial and time-mean over 20 years of daily data over the continental shelf where the ASC is located, and the comparison between experimental and theoretical  $E_0$  as wind and bottom drag are varied is shown in Figure 9 (c) and (d). We see that as  $\tau_x$  is increased the  $E_0$  for channel model simulations increases in magnitude, matching the prediction by the low-order model. Channel model simulations have a decreasing magnitude of  $E_0$  by 10% over a tripling of bottom drag, while the low-order model predicts that  $E_0$  will remain constant. The equilibrium  $APE_0$  in simulations is also compared with the low-order model prediction in Figure 9 (e) and (f), as wind stress and bottom drag are varied. The low-order model shows  $APE_0$  increasing with bottom drag but is independent of wind stress. Although the variation of wind stress is not predicted to have any effect on  $APE_0$ , we find in the simulations that  $APE_0$  increases significantly as wind stress is increased (Figure 9 (e)). In the channel model

simulations,  $APE_0$  increases as bottom drag increases, although at a slower rate compared to  $APE_0$  in the low-order model (Figure 9 (f)).

These discrepancies in equilibrium energies between the low-order model and channel model simulations are significant and could be due to a number of the assumptions in the low-order model, such as: 1) the channel model simulations use a quadratic drag, while the low-order model uses a linear drag, as addressed earlier in the section; 2) the assumption that the rate of eddy energy generation is directly proportional to eddy energy and vertical shear is an oversimplification, and; 3) the low-order model assumes a flat-bottom channel while the channel model simulations have a continental slope. These could contribute to the difference in trends seen in Figure 9 (d), (e) and (f). Considering that the effect of the continental slope is excluded from the low-order model, the parallels between the low-order model and the channel model simulations already illustrate key similarities between the systems, especially in the trend in period of oscillation as wind stress and bottom drag are varied.

Comparisons between the low-order model and the channel model simulations indicate that these systems share similar underlying dynamics, allowing us to draw comparisons. Both systems exhibit energy exchanges between  $APE$  and  $E$ , with  $APE$  acting as the source of energy for  $E$ , as enhanced eddy activity acts to flatten the isopycnals. This cycle of  $APE$  gain and loss drives the temporal variability of  $E$  and the ASC strength. The timescale of this energy exchange is independent of the timescale of external forcings, as the low-order model and the simulated ASC have constant wind forcing applied to the system. The low-order model therefore verifies that the simulated ASC system in the fresh shelf regime is intrinsically oscillatory.

## 5. Discussion and conclusions

We develop an idealised configuration of the ASC in a fresh shelf regime to demonstrate that canyons play a key role in the episodic cross-slope transport of warm CDW water. A cycle of rising and falling rates of eddy generation leads to a temporal variability in ASC strength and eddy kinetic energy in the flow. This temporal variability in eddy energy and ASC strength allows for episodic CDW intrusions on to the continental shelf via canyons, as a weakened current results in an uplift of isopycnals, facilitating the transport of eddies and CDW onto the continental shelf. We also assess the importance of canyon width on CDW transport; wider canyons allow for a greater transport of CDW onto the shelf with distinct episodes of intrusion at a regular frequency, while narrower canyons result in greater asymmetry between the draining and isolated pulses of warm CDW intrusions onto the shelf.

We additionally find that the temporal variability of CDW intrusions and the ASC is intrinsic to the ASC system, as it is present even without any external time-varying forcings applied. The intrinsic variability exists as a consequence of the feedbacks between wind energy input and eddy generation. This relationship is supported by a low-order model of the ASC, which exhibits similar behaviour to the isopycnal channel model simulations. In the low-order model, an intrinsically, temporally-varying current system is set up, as a regular cycle of energy gain and loss occurs; available potential energy is converted to eddy energy and dissipated, before potential energy is generated again as wind forcing continues to act on the system. The result that baroclinic instability is the dominant cause of variability in the modelled ASC comes with a caveat; this is an idealised model with constant forcings and thus does not impose any variability or other water mass transformations. Hence, baroclinic instability may play a different role in the variability of CDW intrusions seen in more realistic models and in observations.

There are currently few realistic modelling studies or observations of the ASC in the East Antarctic, which limits our understanding of the intrinsic variability in the ASC system. Regional simulations of the Totten Glacier region with time-varying external wind forcings have shown a temporal variability in ASC strength, with strong ASC weakening events occurring about every 10 years, but also a higher frequency variability on the order of years (Nakayama et al. 2021). Direct observations of the ASC in East Antarctica have primarily observed higher-frequency variability in ASC strength (Peña-Molino et al. 2016), however, these observed time-series are shorter than two years, which would not be able to capture biennial oscillations in ASC strength. In regional models and observations, the presence of high frequency variability, irregular topography and time-varying external forcings, possibly with interannual variability, make isolating a dominant frequency of intrinsic oscillation in ASC strength difficult to detect. Further work could apply the physical understanding of the ASC, gained from using the low-order model, to realistic models and observations and diagnose the intrinsic variability that we see in the channel model simulations. New observation programs could also target longer periods of continuous measurements, such that interannual variability in the ASC and CDW intrusions could be captured in observations. Observing and understanding this intrinsic variability can significantly improve our knowledge of how CDW intrusions onto the shelf occur, which in turn would be important for predicting basal melt rates on the Antarctic continental shelf. In addition, with the latest climate model projections suggesting a weakening of the coastal easterly winds over the coming century (Neme et al. 2022), our findings suggest projected changes in winds over East Antarctica would have implications for both ASC strength and CDW intrusions in the future.

Although our idealised configuration captures the basic structure of the fresh shelf regime, there exist limitations to our study. The isopycnal model cannot, for example, capture the effects of water mass transformations, and hence cannot address issues such as the effect of a freshened shelf via additional meltwater on the ASC (Moorman et al. 2020; Si et al. 2022a,b). In addition, the effects of sea ice and tides are not included in this model (Si et al. 2022a,b; Stewart et al. 2019). The effect of varying canyon topography on cross-shelf dynamics, including the effects of canyon length, steepness of canyon slope, and continental slope steepness, are outside the scope of this study but would be useful future work, as previous studies have highlighted the importance of these factors on the dynamics on a continental slope (Zhang et al. 2011; Stern et al. 2015; Daae et al. 2017; Han et al. 2022). A previous study has also demonstrated the effects of varying wind strength on CDW intrusions on the Weddell Sea continental shelf (Daae et al. 2017). Motivated by projected weakening of coastal easterlies (Neme et al. 2022), assessing the impact of wind strength changes on CDW intrusions around the East Antarctic is an important area of future work.

The low-order model of the ASC and its oscillatory solution for energy captures the key energetic exchanges of the system, but there are parameters that affect the oscillatory behaviour that have not been explored fully. Topography and the continental slope are not represented in the low-order model, for example, even though they play a significant role in current dynamics on continental slopes (e.g. Isachsen 2011; Stern et al. 2015; Bai et al. 2021; Si et al. 2022b). Additionally, other parameters such as stratification and current width have an additional coupled effect not captured in the low-order model. According to the low-order model prediction (8), stratification and current width have opposing effects on the period of eddy energy oscillation, but the direct effect of each parameter on the oscillation period is not consistent with the channel model simulations as there are other compensating mechanisms present. Instead in our channel model simulations, stratification and current width are coupled to each other, e.g. a narrower current is formed as stratification is reduced (not shown). Hence, to predict the period of oscillation using the low-order model, the stratification and current width variables in (8) both have to be modified. The criterion required for this oscillation to occur has also not been determined, but previous work in similar setups have pointed to the existence of a critical threshold for which periodic behaviour in a jet can occur (Hogg and Blundell 2006; Chekroun et al. 2022). Understanding the criteria required and the experimental parameters key to inducing this oscillatory behaviour in the ASC would be a compelling area of future research, and could also be applied to other boundary current systems globally.

Our idealised representation of the ASC captures a previously unknown feature of CDW intrusions and ASC

strength: namely, their intrinsic temporal variability and the direct causal link between ASC weakening and CDW intruding onto the continental shelf, via baroclinic instability and eddy generation. We conclude that a time-varying external forcing is not required to force interannual variability in ASC strength and CDW intrusions. There could thus be additional variability in CDW intrusions not captured in non-eddy resolving models. Further work could assess the conditions required for the intrinsic variability to occur and diagnose this variability in realistic models and observations in an effort to improve our understanding of CDW intrusions around East Antarctica.

**Acknowledgments.** This research was supported by the Australian Research Council Special Research Initiative, Australian Centre for Excellence in Antarctic Science (ARC Project Number SR200100008). E.Q.Y.O. is supported by the Australian Government Research Training Program Scholarship (RTP). N.C.C. is supported by the Australian Research Council DECRA Fellowship DE210100749. A.McC.H. and M.H.E. (DP190100494) acknowledge funding from the Australian Research Council. This project received grant funding from the Australian Government as part of the Antarctic Science Collaboration Initiative program (ASCI00002). Computational resources were provided by the Australian National Computational Infrastructure at the ANU, which is supported by the Commonwealth Government of Australia.

**Data availability statement.** Scripts used for analysis and for reproducing figures will be available at <https://github.com/ongqingyee/idealised-ASC> upon acceptance of this manuscript. The source code for the MOM6 simulation run is available on <https://github.com/mom-ocean/MOM6>. Simulation data to reproduce figures will be available in a Zenodo repository upon acceptance of the manuscript.

## References

- Adcroft, A., and Coauthors, 2019: The GFDL Global Ocean and Sea Ice Model OM4.0: Model Description and Simulation Features. *Journal of Advances in Modeling Earth Systems*, **11** (10), 3167–3211, <https://doi.org/10.1029/2019MS001726>.
- Aiki, H., X. Zhai, and R. J. Greatbatch, 2016: Energetics Of The Global Ocean: The Role Of Mesoscale Eddies. *Indo-Pacific Climate Variability and Predictability*, Vol. 7, chap. 4, 109–134, [https://doi.org/10.1142/9789814696623\\_0004](https://doi.org/10.1142/9789814696623_0004).
- Bai, Y., Y. Wang, and A. L. Stewart, 2021: Does Topographic Form Stress Impede Prograde Ocean Currents? *Journal of Physical Oceanography*, **51** (8), 2617–2638.
- Chekroun, M. D., H. Dijkstra, T. Şengül, and S. Wang, 2022: Transitions of zonal flows in a two-layer quasi-geostrophic ocean model. *Nonlinear Dynamics*, **109** (3), 1887–1904, <https://doi.org/10.1007/s11071-022-07529-w>.

- Constantinou, N. C., and A. M. C. Hogg, 2019: Eddy Saturation of the Southern Ocean: A Baroclinic Versus Barotropic Perspective. *Geophysical Research Letters*, **46** (21), 12 202–12 212, <https://doi.org/10.1029/2019GL084117>.
- Daae, K., T. Hattermann, E. Darelius, and I. Fer, 2017: On the effect of topography and wind on warm water inflow—An idealized study of the southern Weddell Sea continental shelf system. *Journal of Geophysical Research: Oceans*, **122** (3), 2622–2641, <https://doi.org/10.1002/2016JC012541>.
- Daae, K., T. Hattermann, E. Darelius, R. D. Mueller, K. A. Naughten, R. Timmermann, and H. H. Hellmer, 2020: Necessary Conditions for Warm Inflow Toward the Filchner Ice Shelf, Weddell Sea. *Geophysical Research Letters*, **47** (22), <https://doi.org/10.1029/2020GL089237>.
- Darelius, E., I. Fer, and K. W. Nicholls, 2016: Observed vulnerability of Filchner-Ronne Ice Shelf to wind-driven inflow of warm deep water. *Nature Communications*, **7**, <https://doi.org/10.1038/ncomms12300>.
- Darelius, E., K. Makinson, K. Daae, I. Fer, P. R. Holland, and K. W. Nicholls, 2014: Hydrography and circulation in the Filchner Depression, Weddell Sea, Antarctica. *Journal of Geophysical Research C: Oceans*, **119** (9), 5797–5814, <https://doi.org/10.1002/2014JC010225>.
- DeConto, R. M., and D. Pollard, 2016: Contribution of Antarctica to past and future sea-level rise. *Nature*, **531** (7596), 591–597, <https://doi.org/10.1038/nature17145>.
- Depoorter, M. A., J. L. Bamber, J. A. Griggs, J. T. Lenaerts, S. R. Ligtenberg, M. R. Van Den Broeke, and G. Moholdt, 2013: Calving fluxes and basal melt rates of Antarctic ice shelves. *Nature*, **502** (7469), 89–92, <https://doi.org/10.1038/nature12567>.
- Gudmundsson, G. H., F. S. Paolo, S. Adusumilli, and H. A. Fricker, 2019: Instantaneous Antarctic ice sheet mass loss driven by thinning ice shelves. *Geophysical Research Letters*, **46** (23), 13 903–13 909, <https://doi.org/10.1029/2019GL085027>.
- Gwyther, D. E., B. K. Galton-Fenzi, J. R. Hunter, and J. L. Roberts, 2014: Simulated melt rates for the Totten and Dalton ice shelves. *Ocean Science*, **10** (3), 267–279, <https://doi.org/10.5194/os-10-267-2014>.
- Gwyther, D. E., T. J. O’Kane, B. K. Galton-Fenzi, D. P. Monselesan, and J. S. Greenbaum, 2018: Intrinsic processes drive variability in basal melting of the Totten Glacier Ice Shelf. *Nature Communications*, **9** (1), <https://doi.org/10.1038/s41467-018-05618-2>.
- Han, X., A. L. Stewart, D. Chen, T. Lian, X. Liu, and X. Xie, 2022: Topographic Rossby Wave-Modulated Oscillations of Dense Overflows. *Journal of Geophysical Research: Oceans*, **127** (9), <https://doi.org/10.1029/2022JC018702>.
- Hattermann, T., L. H. Smedsrød, O. A. Nøst, J. M. Lilly, and B. K. Galton-Fenzi, 2014: Eddy-resolving simulations of the Fimbul Ice Shelf cavity circulation: Basal melting and exchange with open ocean. *Ocean Modelling*, **82**, 28–44, <https://doi.org/10.1016/j.ocemod.2014.07.004>.
- Herraiz-Borreguero, L., J. A. Church, I. Allison, B. Peña-Molino, R. Coleman, M. Tomczak, and M. Craven, 2016: Basal melt, seasonal water mass transformation, ocean current variability, and deep convection processes along the Amery Ice Shelf calving front, East Antarctica. *Journal of Geophysical Research: Oceans*, **121** (7), 4946–4965, <https://doi.org/10.1002/2016JC011858>.
- Herraiz-Borreguero, L., and A. C. Naveira Garabato, 2022: Poleward shift of Circumpolar Deep Water threatens the East Antarctic Ice Sheet. *Nature Climate Change*, **12** (8), 728–734, <https://doi.org/10.1038/s41558-022-01424-3>.
- Heywood, K. J., and Coauthors, 2014: Ocean processes at the Antarctic continental slope. *Philosophical Transactions of the Royal Society A: Mathematical, Physical and Engineering Sciences*, **372** (2019), <https://doi.org/10.1098/rsta.2013.0047>.
- Hirano, D., and Coauthors, 2020: Strong ice-ocean interaction beneath Shirase Glacier Tongue in East Antarctica. *Nature Communications*, **11** (1), <https://doi.org/10.1038/s41467-020-17527-4>.
- Hogg, A. M. C., and J. R. Blundell, 2006: Interdecadal Variability of the Southern Ocean. *Journal of Physical Oceanography*, **36** (8), 1626–1645, <https://doi.org/10.1175/JPO2934.1>.
- Huneke, W. G. C., A. Klocke, and B. K. Galton-Fenzi, 2019: Deep bottom mixed layer drives intrinsic variability of the antarctic slope front. *Journal of Physical Oceanography*, **49** (12), 3163–3177, <https://doi.org/10.1175/JPO-D-19-0044.1>.
- Huneke, W. G. C., A. K. Morrison, and A. M. Hogg, 2022: Spatial and Subannual Variability of the Antarctic Slope Current in an Eddying Ocean–Sea Ice Model. *Journal of Physical Oceanography*, **52** (3), 347–361, <https://doi.org/10.1175/JPO-D-21-0143.1>.
- Isachsen, P. E., 2011: Baroclinic instability and eddy tracer transport across sloping bottom topography: How well does a modified Eady model do in primitive equation simulations? *Ocean Modelling*, **39** (1–2), 183–199, <https://doi.org/10.1016/j.ocemod.2010.09.007>.
- Kiss, A. E., and Coauthors, 2020: ACCESS-OM2 v1.0: A global ocean-sea ice model at three resolutions. *Geoscientific Model Development*, **13** (2), 401–442, <https://doi.org/10.5194/gmd-13-401-2020>.
- Liu, C., Z. Wang, C. Cheng, R. Xia, B. Li, and Z. Xie, 2017: Modeling modified Circumpolar Deep Water intrusions onto the Prydz Bay continental shelf, East Antarctica. *Journal of Geophysical Research: Oceans*, **122** (7), 5198–5217, <https://doi.org/10.1002/2016JC012336>.
- Liu, C., Z. Wang, X. Liang, X. Li, X. Li, C. Cheng, and D. Qi, 2022: Topography-Mediated Transport of Warm Deep Water across the Continental Shelf Slope, East Antarctica. *Journal of Physical Oceanography*, <https://doi.org/10.1175/JPO-D-22-0023.1>.
- Marshall, D. P., M. H. Ambaum, J. R. Maddison, D. R. Munday, and L. Novak, 2017: Eddy saturation and frictional control of the Antarctic Circumpolar Current. *Geophysical Research Letters*, **44** (1), 286–292, <https://doi.org/10.1029/2016GL071702>.
- Marshall, D. P., J. R. Maddison, and P. S. Berloff, 2012: A framework for parameterizing eddy potential vorticity fluxes. *Journal of Physical Oceanography*, **42** (4), 539–557, <https://doi.org/10.1175/JPO-D-11-048.1>.
- Moorman, R., A. K. Morrison, and A. M. C. Hogg, 2020: Thermal Responses to Antarctic Ice Shelf Melt in an Eddy-Rich Global Ocean–Sea Ice Model. *Journal of Climate*, **33** (15), 6599–6620, <https://doi.org/10.1175/JCLI-D-19-0846.1>.
- Morlighem, M., and Coauthors, 2020: Deep glacial troughs and stabilizing ridges unveiled beneath the margins of the Antarctic ice sheet. *Nature Geoscience*, **13** (2), 132–137, <https://doi.org/10.1038/s41561-019-0510-8>.

- Morrison, A. K., A. M. Hogg, M. H. England, and P. Spence, 2020: Warm Circumpolar Deep Water transport toward Antarctica driven by local dense water export in canyons. *Science Advances*, **6** (18), <https://doi.org/10.1126/sciadv.aav2516>.
- Munk, W. H., and E. Palmén, 1951: Note on the Dynamics of the Antarctic Circumpolar Current. *Tellus*, **3** (1), 53–55, <https://doi.org/10.3402/tellusa.v3i1.8609>.
- Nakayama, Y., and Coauthors, 2021: Antarctic Slope Current Modulates Ocean Heat Intrusions Towards Totten Glacier. *Geophysical Research Letters*, **48** (17), <https://doi.org/10.1029/2021GL094149>.
- Neme, J., M. H. England, and A. McC. Hogg, 2022: Projected Changes of Surface Winds Over the Antarctic Continental Margin. *Geophysical Research Letters*, **49** (16), <https://doi.org/10.1029/2022GL098820>.
- Nitsche, F. O., D. Porter, G. Williams, E. A. Cougnon, A. D. Fraser, R. Correia, and R. Guerrero, 2017: Bathymetric control of warm ocean water access along the East Antarctic Margin. *Geophysical Research Letters*, **44** (17), 8936–8944, <https://doi.org/10.1002/2017GL074433>.
- NOAA National Geophysical Data Center, 2009: ETOPO1 1 Arc-Minute Global Relief Model. NOAA National Centers for Environmental Information, <https://doi.org/doi:10.7289/V5C8276M>.
- Nøst, O. A., M. Biuw, V. Tverberg, C. Lydersen, T. Hattermann, Q. Zhou, L. H. Smedsrød, and K. M. Kovacs, 2011: Eddy overturning of the Antarctic Slope Front controls glacial melting in the Eastern Weddell Sea. *Journal of Geophysical Research: Oceans*, **116** (11), <https://doi.org/10.1029/2011JC006965>.
- Ohshima, K. I., and Coauthors, 2013: Antarctic Bottom Water production by intense sea-ice formation in the Cape Darnley polynya. *Nature Geoscience*, **6** (3), 235–240, <https://doi.org/10.1038/ngeo1738>.
- Paolo, F. S., H. A. Fricker, and L. Padman, 2015: Volume loss from Antarctic ice shelves is accelerating. *Science*, **348** (6232), 327–331, <https://doi.org/10.1126/science.aaa0940>.
- Peña-Molino, B., M. S. McCartney, and S. R. Rintoul, 2016: Direct observations of the Antarctic Slope Current transport at 113°E. *Journal of Geophysical Research: Oceans*, **121** (10), 7390–7407, <https://doi.org/10.1002/2015JC011594>.
- Ribeiro, N., L. Herráiz-Borreguero, S. R. Rintoul, C. R. McMahon, M. Hindell, R. Harcourt, and G. Williams, 2021: Warm Modified Circumpolar Deep Water Intrusions Drive Ice Shelf Melt and Inhibit Dense Shelf Water Formation in Vincennes Bay, East Antarctica. *Journal of Geophysical Research: Oceans*, **126** (8), <https://doi.org/10.1029/2020JC016998>.
- Rignot, E., Jérémie Mouginot, B. Scheuchl, M. Van Den Broeke, M. J. Van Wessem, M. Morlighem, R. R. Forster, and L. A. Stearns, 2019: Four decades of Antarctic Ice Sheet mass balance from 1979–2017. *Proceedings of National Academy of Sciences*, **116** (4), 1095–1103, <https://doi.org/10.1073/pnas.1812883116>.
- Rintoul, S. R., A. Silvano, B. Peña-Molino, E. van Wijk, M. Rosenberg, J. S. Greenbaum, and D. D. Blankenship, 2016: Ocean heat drives rapid basal melt of the Totten Ice Shelf. *Science Advances*, **2** (12), <https://doi.org/10.1126/sciadv.1601610>.
- Si, Y., A. L. Stewart, and I. Eisenman, 2022a: Coastal freshening enhances eddy-driven heat transfer toward the Antarctic margins. (*preprint*), <https://doi.org/10.1002/essoar.10510349.1>.
- Si, Y., A. L. Stewart, and I. Eisenman, 2022b: Coupled ocean/sea ice dynamics of the Antarctic Slope Current driven by topographic eddy suppression and sea ice momentum redistribution. *Journal of Physical Oceanography*, **52** (7), 1563–1589, <https://doi.org/10.1175/JPO-D-21-0142.1>.
- Silvano, A., S. R. Rintoul, K. Kusahara, B. Peña-Molino, E. van Wijk, D. E. Gwyther, and G. D. Williams, 2019: Seasonality of Warm Water Intrusions Onto the Continental Shelf Near the Totten Glacier. *Journal of Geophysical Research: Oceans*, **124** (6), 4272–4289, <https://doi.org/10.1029/2018JC014634>.
- Silvano, A., S. R. Rintoul, B. Peña-Molino, W. R. Hobbs, E. Van Wijk, S. Aoki, T. Tamura, and G. D. Williams, 2018: Freshening by glacial meltwater enhances melting of ice shelves and reduces formation of Antarctic Bottom Water. *Science Advances*, **4** (4).
- St-Laurent, P., J. M. Klinck, and M. S. Dinniman, 2013: On the role of coastal troughs in the circulation of warm circumpolar deep water on Antarctic shelves. *Journal of Physical Oceanography*, **43** (1), 51–64, <https://doi.org/10.1175/JPO-D-11-0237.1>.
- Stern, A., L. P. Nadeau, and D. Holland, 2015: Instability and mixing of zonal jets along an idealized continental shelf break. *Journal of Physical Oceanography*, **45** (9), 2315–2338, <https://doi.org/10.1175/JPO-D-14-0213.1>.
- Stewart, A. L., A. Klocker, and D. Menemenlis, 2019: Acceleration and overturning of the Antarctic Slope Current by winds, eddies, and tides. *Journal of Physical Oceanography*, **49** (8), 2043–2074, <https://doi.org/10.1175/JPO-D-18-0221.1>.
- Stewart, A. L., and A. F. Thompson, 2015: Eddy-mediated transport of warm Circumpolar Deep Water across the Antarctic Shelf Break. *Geophysical Research Letters*, **42** (2), 432–440, <https://doi.org/10.1002/2014GL062281>.
- Stewart, A. L., and A. F. Thompson, 2016: Eddy generation and jet formation via dense water outflows across the Antarctic continental slope. *Journal of Physical Oceanography*, **46** (12), 3729–3750, <https://doi.org/10.1175/JPO-D-16-0145.1>.
- Stokes, C. R., and Coauthors, 2022: Response of the East Antarctic Ice Sheet to past and future climate change. *Nature*, **608** (7922), 275–286, <https://doi.org/10.1038/s41586-022-04946-0>.
- Thompson, A. F., K. J. Heywood, S. Schmidtko, and A. L. Stewart, 2014: Eddy transport as a key component of the Antarctic overturning circulation. *Nature Geoscience*, **7** (12), 879–884, <https://doi.org/10.1038/ngeo2289>.
- Thompson, A. F., A. L. Stewart, P. Spence, and K. J. Heywood, 2018: The Antarctic Slope Current in a Changing Climate. *Reviews of Geophysics*, **56** (4), 741–770, <https://doi.org/10.1029/2018RG000624>.
- Williams, G. D., S. Aoki, S. S. Jacobs, S. R. Rintoul, T. Tamura, and N. L. Bindoff, 2010: Antarctic Bottom Water from the Adélie and George V Land coast, East Antarctica (140–149°E). *Journal of Geophysical Research*, **115** (C4), C04 027, <https://doi.org/10.1029/2009JC005812>.
- Young, W. R., 2012: An exact thickness-weighted average formulation of the boussinesq equations. *Journal of Physical Oceanography*, **42** (5), 692–707, <https://doi.org/10.1175/JPO-D-11-0102.1>.
- Yung, C. K., A. K. Morrison, and A. M. Hogg, 2022: Topographic Hotspots of Southern Ocean Eddy Upwelling. *Frontiers in Marine Science*, **9**, <https://doi.org/10.3389/fmars.2022.855785>, URL <https://www.frontiersin.org/articles/10.3389/fmars.2022.855785/full>.

Zhang, Y., J. Pedlosky, and G. R. Flierl, 2011: Shelf circulation and cross-shelf transport out of a bay driven by eddies from an open-ocean current. Part I: Interaction between a barotropic vortex and a steplike topography. *Journal of Physical Oceanography*, **41** (5), 889–910, <https://doi.org/10.1175/2010JPO4496.1>.

## APPENDIX

### Derivation of Coupled Ordinary Differential Equations for Total Eddy Energy and Available Potential Energy in Low-Order Model

We express the eddy budget in (2) and (3) in terms of the depth-integrated total available potential energy per unit longitudinal length,  $APE$ , and the depth-integrated total eddy energy per unit longitudinal length,  $E$ . We first define  $APE$  in this two-layered model; see Figure 7. We have one free interface between the two fluid layers,  $\eta(y)$ , a rigid lid and define the thickness of each layer as  $h_i$ . We assume the slope of the density interface is constant within the model domain, such that  $\eta = \text{sgn}(\tau_x)\text{sgn}(f)sy$ , where  $s > 0$  is the magnitude of the slope of the density interface. The sign of the slope,  $\partial\eta/\partial y$ , depends on the sign of the wind stress and the Coriolis parameter. In a domain of latitudinal length  $L_y$ , over which the slope of the density surface is constant, the  $APE$  is:

$$\begin{aligned} APE &= \int_0^{L_y} \frac{1}{2} \rho_0 g' \eta^2 dy \\ &= \frac{1}{6} \rho_0 g' s^2 L_y^3, \end{aligned} \quad (\text{A1})$$

where  $\rho_0$  is the reference density and  $g' = g\Delta\rho/\rho_0$  is reduced gravity of the two-layer system.

Defining the eddy energy conversion term as  $|f|/N|\partial u/\partial z|E$  (Marshall et al. 2012, 2017), where  $E = \sum_i \int (\frac{1}{2}\rho_0 h_i |\mathbf{u}_i''|^2 + \frac{1}{2}\rho_0 g' \eta''^2) dy$ , we can find an expression for this term using the parameters of the layered model. We define the vertical shear  $\partial u/\partial z$  discretely as  $\partial u/\partial z = (u_1 - u_2)/(H/2)$ , setting the bottom velocity  $u_{\text{bot}} = 0$  and surface velocity as  $u_{\text{surface}} = H\partial u/\partial z = 2(u_1 - u_2)$ , assuming constant linear shear. To remove the velocity terms in each layer, we use the thermal wind balance  $f(u_1 - u_2) = g'\partial\eta/\partial y = \text{sgn}(\tau_x)\text{sgn}(f)g's$  and combine all the terms above to write the expressions for the rate of change of depth-integrated eddy energy in terms of  $APE$  to arrive at (4).

Next, we define the rate of change of  $APE$ , the energy input from winds as  $\iint \boldsymbol{\tau} \cdot \mathbf{u}_{\text{surface}} dA$ . If we consider only the zonal flow component, the work per unit longitude is:

$$\text{Wind Input} = \int \tau_x u_{\text{surface}} dy. \quad (\text{A2})$$

To express the wind energy input in terms of  $APE$  and  $E$ , we use the surface velocity  $u_{\text{surface}} = 2(u_1 - u_2)$  and find

the zonal velocities in individual layers through geostrophy to express the wind energy input in terms of the slope of the density interface:

$$u_{1g} = \frac{-1}{\rho_0 f} \frac{\partial p_{\text{atm}}}{\partial y}, \quad (\text{A3})$$

$$u_{2g} = -\frac{1}{\rho_0 f} \left( \frac{\partial p_{\text{atm}}}{\partial y} + g' \rho_0 \frac{\partial \eta}{\partial y} \right), \quad (\text{A4})$$

which when combined give:

$$u_{\text{surface}} = 2(u_{1g} - u_{2g}) = \text{sgn}(\tau_x) \frac{2g's}{|f|}. \quad (\text{A5})$$

Substituting the expression for  $u_{\text{surface}}$  into (A2), using (A1) to write  $s$  in terms of  $APE$ , and using the same eddy energy conversion term as for (4), we end up with (5).